

Testing Convergence of Cosmological Simulations with GADGET-4

AARON OUELLETTE  ¹

¹ Department of Physics, University of Illinois Urbana-Champaign, Urbana IL 61801

ABSTRACT

Large N-body simulations have become an extremely important part of modern cosmology. These simulations allow us to compare observations from modern large-scale surveys directly to theory predictions as well as fully model the physical effects we expect to see in observations. Thus, it is extremely important to fully understand all of the parameter choices that go into running these simulations to ensure that they properly converge and accurately describe the real universe. In this paper I study the effects of discreteness parameters in cosmological N-body simulations on various cosmological observables, specifically in the context of fixed cosmological parameters and using the new GADGET-4 code. I provide motivation for the various choices one can make for values of N and the box size L and I determine the optimal value of the softening length ϵ to avoid unphysical close encounters while preserving small-scale resolution.

Keywords: N-body simulations (1083), Large-scale structure of the universe (902), Cosmology (343)

1. INTRODUCTION

Our current understanding of cosmology is best described by a flat Λ CDM model with $\Omega_m \approx 0.3$, $H_0 \approx 67 \text{ km s}^{-1} \text{ Mpc}^{-1}$, and initial density variations arising from quantum fluctuations directly after inflation. The name Λ CDM stands for the dominant components of the universe today: dark energy in the form of a cosmological constant (Λ) and cold (meaning non-relativistic) dark matter (DM). All other components such as radiation, baryonic matter, neutrinos, etc. comprise approximately 5% of the current total energy density of the universe. While looming questions still remain (such as the Hubble tension (Verde et al. 2019) and the fundamental natures of dark matter and dark energy), this model is well supported by a wealth of observations. This includes: anisotropies in the cosmic microwave background (Planck Collaboration et al. 2020), distance measurements from supernovae (Riess et al. 2021; Brout et al. 2022), galaxy clustering and weak gravitational lensing (Alam et al. 2017; Abbott et al. 2018), and many more. For more details about the fundamentals of cosmology and all of the observational evidence for dark energy see Frieman et al. (2008). Also see Turner (2022) for a recent detailed review of the history of cosmology from the early 1900's to its current state as a precision science.

Computation is one of the three pillars, along with observations and theory, that support our current understanding of cosmology. Simulations provide a direct connection between theory and observations, allowing us to effectively run experiments on the universe. Simulations additionally help us better understand observations by modeling the effects we might expect to see through the creation of mock observations. Additionally, in recent years, there have been major advances on the simulation side of things, both in terms of more powerful hardware available and better software and algorithms. Some examples of simulation codes that have been used to run very large simulations are: HACC (Habib et al. 2016), ABACUS (Garrison et al. 2021a), many different GADGET variants, and many others. All of these codes implement the same core elements of a cosmological simulation, but vary in their implementation details, specific uses, or optimization for certain hardware. These codes can also vary in terms of the extra physics implemented, such as (magneto-)hydrodynamics, star formation, different models of dark matter, etc. Thus, it is important to ensure that different codes provide consistent predictions when modeling the same physical phenomena.

Following are some examples of recent uses of state-of-the-art large-scale cosmological simulations.

- IllustrisTNG (Nelson et al. 2018; Naiman et al. 2018; Springel et al. 2018; Marinacci et al. 2018; Pillepich et al. 2018): a series of simulations aimed at modeling the formation and evolution of galaxies in a cosmological context.
- CosmoDC2 (Korytov et al. 2019): a synthetic sky catalog to help with LSST analysis. CosmoDC2 covers 440 deg² of the sky all the way to $z = 3$ and contains over 2 billion galaxies, each with 551 listed properties. This work was based on the Outer Rim simulation (Heitmann et al. 2019), which is one of the largest cosmological simulations run to-date with over a trillion particles.
- CAMELS project (Villaescusa-Navarro et al. 2021): a set of several thousand N-body and hydrodynamical cosmological simulations that can be used with machine learning to study the connection between cosmology and astrophysics.

Of course, many other large simulations have been used, both to aid with the analysis of observations and to compare theory to real-world observations. Clearly, with the ever increasing size of cosmological simulations and the more stringent requirements for precision from observations, it is extremely important to fully understand the internals of the simulations and all potential sources of error.

The run-time parameters of N-body simulations can be broadly divided into physical ones that describe the actual physics being solved (such as the cosmology) and unphysical ones that go into the methods used to solve the equations describing the physics. Unphysical parameters can be further divided into numerical ones that control the approximations used (such as force calculation and error tolerance for various integrations) and discretization ones (such as the number of particles used, the softening length, and so on). Generally, it is the discretization parameters that can introduce unexpected unphysical effects in the simulation since effectively a new discrete problem is being solved that is different from the original continuous physical model.

Much work has already been done to study the effects of discreteness on N-body simulations. For example, Binney (2004) looked at how discreteness in N-body simulations affects DM halos and found that discreteness has a direct effect on virialization: simulations with fewer particles tend to form cuspier halos. Bagla & Ray (2005) and Power & Knebe (2006) looked at how the finite box size L affects large scale structure. They found that using a finite L effectively introduces a cutoff scale for the amount of large-scale power present in the simulation and that this can still affect the small-scale structures such as DM halos. Power et al. (2003) investigate the convergence of DM halo properties such as the radial density profile and rotation curve. They found that the most stringent requirement for convergence is generally that the number of particles enclosed within the region of interest is large enough that the collisional relaxation time-scale is longer than the age of the universe. Scale-free cosmologies (where summary statistics depend only on one length scale due to self-similarity) are a popular way to test the convergence of simulations. Garrison et al. (2021b) uses self-similarity to determine optimal softening lengths for the ABACUS simulations and Maleuvre et al. (2022) uses self-similarity to determine the accuracy of power spectra measurements from simulations. In general, there is a trade-off between needing a large enough ϵ to avoid close encounters, but a small enough one to obtain a sufficient spatial resolution.

In this paper, I aim to investigate how the various discretization parameters of N-body simulations affect various cosmological observables. Specifically, I look at the box size L , mass resolution m_p , and softening length ϵ given a fixed cosmology. Additionally, I briefly examine the differences between simulation results when using two different methods to generate initial conditions. For this, I employ the new GADGET-4 cosmological N-body/SPH code ¹. This is the latest iteration of the series of GADGET codes written by Volker Springel and includes many new and improved features, including: a built-in initial conditions generator, output of power spectra, built-in on-the-fly group finding, merger trees, lightcone output, and various algorithm improvements. For full implementation details and detailed tests see Springel et al. (2021). Further details and context for the development of GADGET can be found in Springel et al. (2001b); Springel (2005). While many cosmological simulation codes exist that are much more specialized for extremely large simulations of the universe, GADGET has been designed to be more flexible and general purpose in its use. This makes GADGET-4 easier to setup and run and perfect to use for this project.

Following is a brief outline of the structure of the paper. In section 2 I briefly review the details of cosmological N-body simulations. In section 3 I go over the methods used to study the convergence of cosmological simulations. In subsection 3.1 I describe the simulation setups and runs used in this work and in subsection 3.2 I go over the summary

¹ <https://wwwmpa.mpa-garching.mpg.de/gadget4/>

statistics used to compare the results of the simulation runs. In section 4 I confirm that the simulations properly describe a realization of a Λ CDM universe. Finally in section 5 I present the results of this work and discuss the conclusions in section 6.

2. COSMOLOGICAL N-BODY SIMULATIONS

Here I give a brief overview of cosmological N-body simulations and connect the general concepts to the specific implementations in GADGET-4. For a recent, detailed review of cosmological N-body simulations in general see Angulo & Hahn (2022). The aim of cosmological N-body simulations is to directly simulate the growth of large scale structures in the universe from small initial density fluctuations to the formation of galaxies, clusters, and super-clusters that we see today. Very often, cosmological simulations include only DM which makes up about 85% of all of the matter in the universe. Since in the Λ CDM paradigm DM is treated as a slow-moving collisionless fluid that only interacts through gravity, this greatly simplifies the simulations by neglecting any baryonic physics that would have to be described with hydrodynamics, star formation, and more complicated physics.

In broad strokes, a cosmological N-body simulation must be able to: 1) specify a discretization of the physical equations that govern the formation of large scale structure, 2) accurately calculate the gravitational force on each particle in the simulation, and 3) accurately integrate the equations of motion forward in time. Most cosmological simulation codes accomplish this by discretizing the DM fluid as a collection of N particles (hence N-body) that move under the influence of their gravity. The N-body simulation is then effectively solving a discretized version of the Poisson-Vlassov equation that describes the phase space distribution of the collisionless DM. These particles are confined to a box of size L with periodic boundary conditions in order to simulate an infinite universe using a finite representation.

For a standard simulation of a flat Λ CDM universe the mass resolution of this simulation is given by

$$m_p = \Omega_m \rho_c L^3 / N, \quad (1)$$

where $\rho_c = 3H^2/8\pi G$ is the critical density of the universe. This mass resolution puts a limit on the smallest structures that will be present in the simulation. Thus L and N directly limit the regimes that the simulation can probe. We also end up with a trade-off, since we generally want a value of m_p that is as small as possible, while maximizing the value of L for a fixed computational cost which is most directly affected by N .

There is also an inherent length resolution in the simulation even though particle positions can be resolved to machine precision. Due to the fact that we are trying to represent a collisionless fluid as a collection of particles, any collisions or close encounters between particles are purely an artifact of the discretization. Thus, we soften the gravitational force when particles get too close to each other to avoid artificial close encounters. This is usually accomplished through the use of a softening length ϵ , roughly on the order of the mean interparticle spacing $L/N^{1/3}$.

Once we have the discretization in terms of N particles of mass m_p , the actual simulation finally boils down to simply calculating the gravitational force on each of the particles, then using a finite-difference method to update each particle's velocity and position all on top of a background governed by the Friedman equations.

2.1. Initial conditions

Generating initial conditions for cosmological N-body simulations is a essentially a problem of using perturbation theory to calculate particle positions and velocities directly instead of using a N-body simulation. This works, because at early times in the universe the growth of structure is linear, before major gravitational collapse begins. This process is called Lagrangian perturbation theory, because we start with the Lagrangian coordinates of the DM fluid in the form of particles arranged on a uniform grid and then transform to Eulerian coordinates at the initial redshift z_i using perturbation theory. This can be done to arbitrary order, but usually it is either 1st order (the Zel'dovich approximation (Zel'dovich 1970)) or 2nd order (2LPT).

The general formulation is as follows: in comoving coordinates, we can relate the Eulerian coordinates x at z_i to the initial Lagrangian coordinates q by:

$$x(q, z_i) = q + D_+(z_i)\Psi(q), \quad (2)$$

$$\dot{x}(z_i) = \dot{D}_+(t)\Psi(q). \quad (3)$$

Here $D_+(z) = \delta(z)/\delta(z=0)$ is the linear density growth factor which depends only on the cosmological parameters. $\Psi(q)$ is the initial displacement field which depends on the density field at z_i which in turn is sampled from the power spectrum at z_i .

In the Zel'dovich approximation, we approximate $\Psi(q)$ only to first order by setting it directly proportional to the gravitational potential exerted by the density field $\delta(z_i)$ at q . Thus the whole process of generating initial conditions using the Zel'dovich approximation can be summarized as:

1. Initialize N particles on a uniform grid inside a box of size L .
2. Calculate the power spectrum at z_i : $P(k, z_i) = \alpha k^{n_s} T^2(k, z_i)$. The transfer function $T^2(k, z)$ can be calculated directly using Boltzmann solvers such as CAMB² or CLASS³, or estimated using various analytic parameterizations.
3. Generate the initial density field $\delta(z_i)$ by sampling from the power spectrum.
4. Calculate the initial displacements and velocities from $\delta(z_i)$ using ZA and perturb the particles from their grid positions to obtain the initial conditions at z_i .

The Zel'dovich approximation only takes into account local effects when calculating the initial displacements and velocities (since it only depends on the gravitational potential). Scoccimarro (1998); Crocce et al. (2006) have shown that including the 2nd order terms in the Lagrangian perturbation theory significantly improves the initial conditions for N-body simulations by removing transients and allowing the simulations to be started from smaller redshifts. Including these terms is effectively including gravitational tidal effects in the initial conditions in addition to the local gravitational potential.

For the 2nd order approximation, the algorithm to calculate initial conditions is still exactly the same. The only difference is that now we include 2nd order terms in $\Psi(q)$ to represent the tidal effects. All of this is handled automatically by GADGET-4 and initial conditions are generated internally right before the full simulation is started.

2.2. Force calculation

Force calculation is usually the most time-intensive part of any N-body simulation and for N above a few tens of thousands is completely prohibitive to do using direct summation. Instead, we must rely on various approximate methods that provide much better scaling with N . Popular methods for efficient gravitational force calculation are either mesh-based, tree-based, or multipole-based. Mesh-based methods are based on solving Poisson's equation on a mesh in Fourier space and thus depend on the Fast Fourier Transform to achieve its speed. Tree-based and multipole methods essentially create a hierarchical structure

A very popular method of force calculation in cosmological simulations is the tree particle-mesh (treePM) method. Here we use a mesh to calculate long-range forces and a tree to calculate close-range forces.

2.3. Time integration

Once we know the forces on all the particles, we need a finite-difference method to integrate the velocities and positions forward in time. The most common method used is the leapfrog or Stormer-Verlet method which is a 2nd order symplectic time integration method. Additionally, in cosmological simulations, the scale factor a is typically used as the time variable instead of t . This implicitly encodes the expansion of the universe based on the FRLW metric into the integration of particle positions and velocities.

The most significant consideration with time integration is the timestep. The basic leapfrog method is symplectic only when a global timestep is used. But this is clearly impractical for large-scale simulations due to the huge range in time-scales present, from the very short orbital periods inside of clusters, to the very slow moving particles in regions of low density. Thus, in most astrophysical or cosmological simulations, the modified leapfrog algorithm of Quinn et al. (1997) is used that allows the slow moving articles to be decoupled from the very fast moving ones. This also allows for parallelization of the algorithm where each particle has its own timestep.

2.4. Post-processing

For any given cosmology, a N-body simulation provides only a potential realization of the large-scale structures in the universe. This realization is random both due to the initial random density fluctuations used as a realization of the

² <https://camb.info/>

³ <http://class-code.net/>

initial conditions after inflation and due to the inherent chaotic behavior of numerical N-body simulations. Thus, we cannot directly compare the particle-level information between two simulations (ignoring the fact that this is already prohibitive due to the size of the datasets and the fact that we do not have this information observationally). Instead, we must calculate summary statistics that describe statistical properties of the large-scale structure and that can be directly compared with observations of the real universe.

Some examples of these summary statistics are: power spectra, correlation functions (which are the Fourier transforms of power spectra), halo mass functions, halo density profiles, and many others. These summary statistics are designed to provide information about the clustering of matter and the properties of collapsed structures (such as galaxies and galaxy clusters).

3. METHODS

Here I describe the simulation setups and the analysis methods used to study their convergence.

3.1. *Simulations*

To test the convergence of cosmological simulations and determine the effects of discreteness on observable statistics, I ran a total of 14 full simulations with the GADGET-4 code. The full list of all of the runs and their parameters is given in Table 1. All of the runs are DM-only N-body simulations.

All of the runs assume a flat Λ CDM universe with parameters consistent with the Planck 2018 results (Planck Collaboration et al. 2020). The initial conditions are generated from a primordial power spectrum assuming a spectral index of $n_s = 0.965$ and a normalization of $\sigma_8 = 0.811$. The cosmology is given by $\Omega_m = 1 - \Omega_\Lambda = 0.315$ and $h = 0.674$, where the convention $H_0 = 100h \text{ km s}^{-1} \text{ Mpc}^{-1}$ is used. Since GADGET internally uses units with h factored out, I will be using the same units for all quantities in this work. So very careful care has to be taken whenever comparing these quantities to ones not using this convention. See Croton (2013) for more details about this “little-h” convention.

All of the simulations begin at an initial redshift of $z = 63$ with initial conditions generated from the primordial power spectrum using built-in code (based on the older N-GenIC⁴ code). The random seeds and phases for the initial conditions are kept the same for all simulations in order to allow for meaningful comparisons. Each simulation is then run up until the present epoch at $z = 0$ and continued slightly into the future (until $a = 5$).

Data outputs are produced at five values of the scale factor a : 0.25, 0.5, 1.0, 2.0, and 5.0. Each output consists of a particle snapshot file and a halo catalog. The halo catalog contains information about the halos and subhalos identified in the simulation. GADGET-4 is able to do this on-the-fly using a friends-of-friends (FoF) algorithm and the SUBFIND algorithm (Springel et al. 2001a). For this work, a linking parameter $b = 0.2$ was used for the FoF algorithm and a minimum size of 32 particles was imposed on the halos.

These simulations and their chosen parameters are designed to test the effect of discreteness on cosmological observables. The parameters being tested are: box length L , number of particles N , softening length ϵ , and the order (first or second) of perturbation theory used to generate the initial conditions.

Runs 1-4 have increasing values of N for a fixed $L = 256h^{-1} \text{ Mpc}$, while Runs 13-15 have decreasing values of L for a fixed $N = 256^3$. These simulation runs cover values of m_p that range over 3.5 orders of magnitude while also testing the effects of different values of L on the simulation results.

Runs 5-7 are exact copies of Runs 1-3, but use the Zel'dovich approximation instead of 2LPT to generate initial conditions. These runs will test whether 2LPT provides significant improvements in the accuracy of cosmological observables for a given starting redshift.

Runs 8-11 finally test the effects of the softening length ϵ on cosmological observables. Here the softening length ranges from $5h^{-1} \text{ kpc}$ to $45h^{-1} \text{ kpc}$. This range of values should have a noticeable effect on the smallest scales of the simulation.

3.2. *Analysis*

All of the analysis for this work is done using Python. The simulation data can be directly loaded into memory as `numpy` arrays and then after the analysis is done, visualizations of the summary statistics are easily made with `matplotlib`. The following subsections describe the summary statistics used and how to calculate them from the simulation data.

⁴ <https://www.h-its.org/2014/11/05/ngenic-code/>

Table 1. Run parameters of the N-body simulations. Parameters that are not listed (e.g. the cosmology) are listed in the text and are kept constant between all of the runs (Run 12, while initially planned was skipped).

Run #	$L(h^{-1} \text{ Mpc})$	N	$m_p(h^{-1} \text{ M}_\odot)$	IC type	$\epsilon (L/N^{1/3})$	$\epsilon (h^{-1} \text{ kpc})$
1	256	64^3	5.6×10^{12}	2LPT	1/42	95
2	256	128^3	7.0×10^{11}	2LPT	1/42	48
3	256	256^3	8.7×10^{10}	2LPT	1/42	24
4	256	512^3	1.1×10^{10}	2LPT	1/42	12
5	256	64^3	5.6×10^{12}	ZA	1/42	95
6	256	128^3	7.0×10^{11}	ZA	1/42	48
7	256	256^3	8.7×10^{10}	ZA	1/42	24
8	256	256^3	8.7×10^{10}	2LPT	1/200	5
9	256	256^3	8.7×10^{10}	2LPT	1/67	15
10	256	256^3	8.7×10^{10}	2LPT	1/29	35
11	256	256^3	8.7×10^{10}	2LPT	1/22	45
13	512	256^3	7.0×10^{11}	2LPT	1/42	48
14	128	256^3	1.1×10^{10}	2LPT	1/42	12
15	64	256^3	1.4×10^9	2LPT	1/42	6

3.2.1. Power spectra

For a collection of N particles of mass m_i and at positions x_i , the density field is

$$\rho(x) = \frac{1}{N} \sum_i m_i \delta^3(x - x_i). \quad (4)$$

We can then define a density contrast

$$\delta(x) = \frac{\rho(x)}{\langle \rho \rangle} - 1, \quad (5)$$

which has a Fourier transform

$$\delta_k = \frac{1}{M} \sum_i m_i e^{ik \cdot x_i}. \quad (6)$$

The power spectrum of this density field is then estimated by averaging the power of all modes with a length around a given value k :

$$\hat{P}(k) = \langle |\delta_k|^2 \rangle. \quad (7)$$

For any density field described by discrete tracer particles, we also have to take into account the shot noise, since the power spectrum of random uniform distribution of points does not vanish (see for example [Colombi et al. \(2009\)](#)). Instead, we have $P_{shot} = L^3/N$ for particles with equal masses. Then the power spectrum of the underlying density field is

$$P(k) = \hat{P}(k) - P_{shot}. \quad (8)$$

Since the units of $P(k)$ are those of volume, we can also define a dimensionless quantity, the logarithmic band power ([Dodelson 2003](#)):

$$\Delta^2(k) = \frac{k^3 P(k)}{2\pi^2}. \quad (9)$$

GADGET-4 is able to measure the power spectrum of all particles in the simulation and outputs its measurements at each output time. Additionally, GADGET uses a box folding technique to measure the matter power spectrum to values of k much higher than the Nyquist frequency of the base Fourier mesh. This method is described in [Springel](#)

et al. (2018). First the power spectrum is measured for the unmodified periodic box, then two extensions to smaller scales are measured by folding the box on top of itself.

The measured power spectra are then outputted as ASCII text files containing very fine k bins. To get an accurate estimate of the power spectrum of the full range of k values, we have to then re-bin the data produced by GADGET to ensure that each bin contains a minimum number of modes and reduce the statistical noise in the measurement.

3.2.2. Halo mass functions

The halo mass function (HMF) is the cumulative mass distribution of all of the halos identified in the simulation. For analytical predictions, the HMF is usually parameterized as a universal relation of the form

$$\frac{dn(M, z)}{d \log M} = \frac{\rho_m}{M} f\left(\frac{\delta_c}{\sigma(M, z)}\right) \left| \frac{d \log \sigma}{d \log M} \right|, \quad (10)$$

where δ_c is the critical over-density for collapse and σ is the variance of overdensities at the given redshift. The function f can be determined by theory or by fitting to the results of N-body simulations.

The original parameterization of the HMF by Press & Schechter (1974) uses:

$$f(\nu) = \sqrt{\frac{2}{\pi}} \nu e^{-\nu^2/2}. \quad (11)$$

Recently more complex parameterizations have been developed, for example Warren et al. (2006), Tinker et al. (2008), and Angulo et al. (2012).

In this work, I calculate the HMF for each simulation simply by counting the number of halos more massive than a given mass. I then compare this to the Press-Schechter fit computed by CCL.

3.2.3. Correlation functions

The 2-point correlation function $\xi(r)$ can be defined as the excess (compared with a random distribution of particles) probability of finding a second particle a distance r away from a first particle (Peebles 1980). We can write this as:

$$dP = n^2(1 + \xi(r_{12}))dV_1 dV_2, \quad (12)$$

where dP is the probability of finding two particles, one in dV_1 and another one in dV_2 . Given a density field $\rho(x)$, we can also write

$$\langle \rho(x+r)\rho(x) \rangle_x = \langle \rho \rangle^2 [1 + \xi(r)] \quad (13)$$

or

$$\xi(r) = \langle \delta(x)\delta(x+r) \rangle_x. \quad (14)$$

Thus, $\xi(r)$ is also related to the Fourier transform of the power spectrum $P(k)$.

In practice, correlation functions are calculated by counting the number of particle pairs with separations in a specified r bin. For my analysis, I use the Python package `Corrfunc`⁵ that implements very fast, parallel routines to measure clustering statistics.

3.2.4. Halo density profiles

It is a well known result (Navarro et al. 1997) that DM halos in simulations follow the Navarro-Frank-White (NFW) radial density profile given by

$$\rho(r) = \frac{\rho_0}{r/r_s(1+r/r_s)^2}, \quad (15)$$

where ρ_0 and r_s are constants that can be related to the virial mass of the halo. In practice, the density profile of a simulated DM halo will be affected both by the mass resolution and the softening length of the simulation. Thus, the density profiles of halos can be a good measure of the convergence of the simulation.

To measure the density profile of a halo in a simulation, one has to convert a 3D distribution of particles to a density field. I accomplish this using kernel density estimation (KDE). I use a Gaussian kernel with a bandwidth of 0.82ϵ .

⁵ <https://github.com/manodeep/Corrfunc>

This value was picked to get the Gaussian kernel as similar as possible to the kernel used in GADGET to calculate the force softening. I use the routine `stats.gaussian_kde` from SciPy to get a function that can be evaluated at any point to get an estimate of the density at that point. Then, to get a radial density profile, I generate a log-spaced set of r values out to the halo radius and use a Fibonacci spiral to sample points on spheres defined by each of these r values. I then get an average value and the standard deviation of the density at each r value by evaluating the KDE at each of these points.

This measured profile can then be compared to the NFW one by fitting using orthogonal distance regression (ODR) implemented in `scipy.odr` to fit the NFW profile to the sampled density profile. I generate a fit only for the inner parts of the density profiles, since the outer parts are heavily affected by mergers and are not expected to follow the NFW profile.

4. TESTS

To make sure that all of my simulations accurately represent a realization of a Λ CDM universe, I compare the results of the largest simulation (run 4 from Table 1) with the theoretical predictions computed using the LSST DESC Core Cosmology Library (CCL)⁶ (Chisari et al. 2019).

First, I confirm that the density field of the large-scale structure looks as expected. Figure 1 shows the projected density field for a 20 Mpc deep slice at three different output times from Run 4. These slices look just as we would expect, with the recognizable pattern of the cosmic web: dense halos connected by thin filaments and separated by large voids. Additionally, we see the formation of structure over time: as gravitational collapse progresses, structures become more well-defined and the density contrast increases significantly.

Next, I compare the matter power spectrum as measured by GADGET to the theory prediction from CCL. Figure 2 shows the power spectrum at two output snapshots: $a = 0.5$ and $a = 1$. Here we generally see excellent agreement between the measured and predicted power spectra.

The halo mass function for the FoF halos from Run 4 at $a = 0.5$ and $a = 1$ is shown in Figure 3. Here we compare the measured HMF to the analytic fit by Press & Schechter (1974). We see slightly smaller counts of mid-mass halos in the simulation compared with the Press-Schechter HMF, but generally there is excellent agreement. Also, note that we can clearly see the cutoff due to the mass resolution where smaller halos can no longer form.

From all of these plots, we can conclude that the largest simulation does indeed do a good job at reproducing the expected features of a Λ CDM universe. Next, we will be comparing the results of all the other simulations to these results to identify the effects of discreteness and lower resolution.

5. RESULTS

In the following subsections, I present the results of the results of comparing the summary statistics for four different groups of the simulation runs. In subsection 5.1, I go over Runs 1-4 which compare different values of N . In subsection 5.2, I go over Runs 13-15 which compare different values of L . These 8 runs together represent the full range of mass resolution tested in these simulations. In subsection 5.3, I go over Runs 5-7 which are exactly the same as Runs 1-3, except that they use the ZA instead of 2LPT to generate initial conditions. Finally, in subsection 5.4, I go over Runs 8-12 which compare different values of the softening length ϵ .

5.1. Number of particles

Simulation runs 1-4 correspond to values of N of 64^3 , 128^3 , 256^3 , and 512^3 respectively. Figure 4 shows density slices for each of these runs for easy visual comparison. We see that, as expected, each run simulates the same realization of large-scale structure, simply in different levels of resolution. Additionally, in the lowest level of resolution, we start to see artifacts left over from the initial grid positions of particles. These artifacts are especially visible in regions of lower density where particles tend to arrange themselves along slightly distorted grid lines.

In Figure 5 we compare the power spectra measured by GADGET for each of these runs to the theory prediction computed with CCL. In general, we see excellent agreement between the measurements and the theory prediction. As N increases, the range over which we can measure the power spectrum increases due to the increase in the Nyquist frequency and the decrease in the shot noise present. We also see that for values of k between ≈ 1 and ≈ 10 the measurements get closer to the theory as N increases.

⁶ <https://github.com/LSSTDESC/CCL>

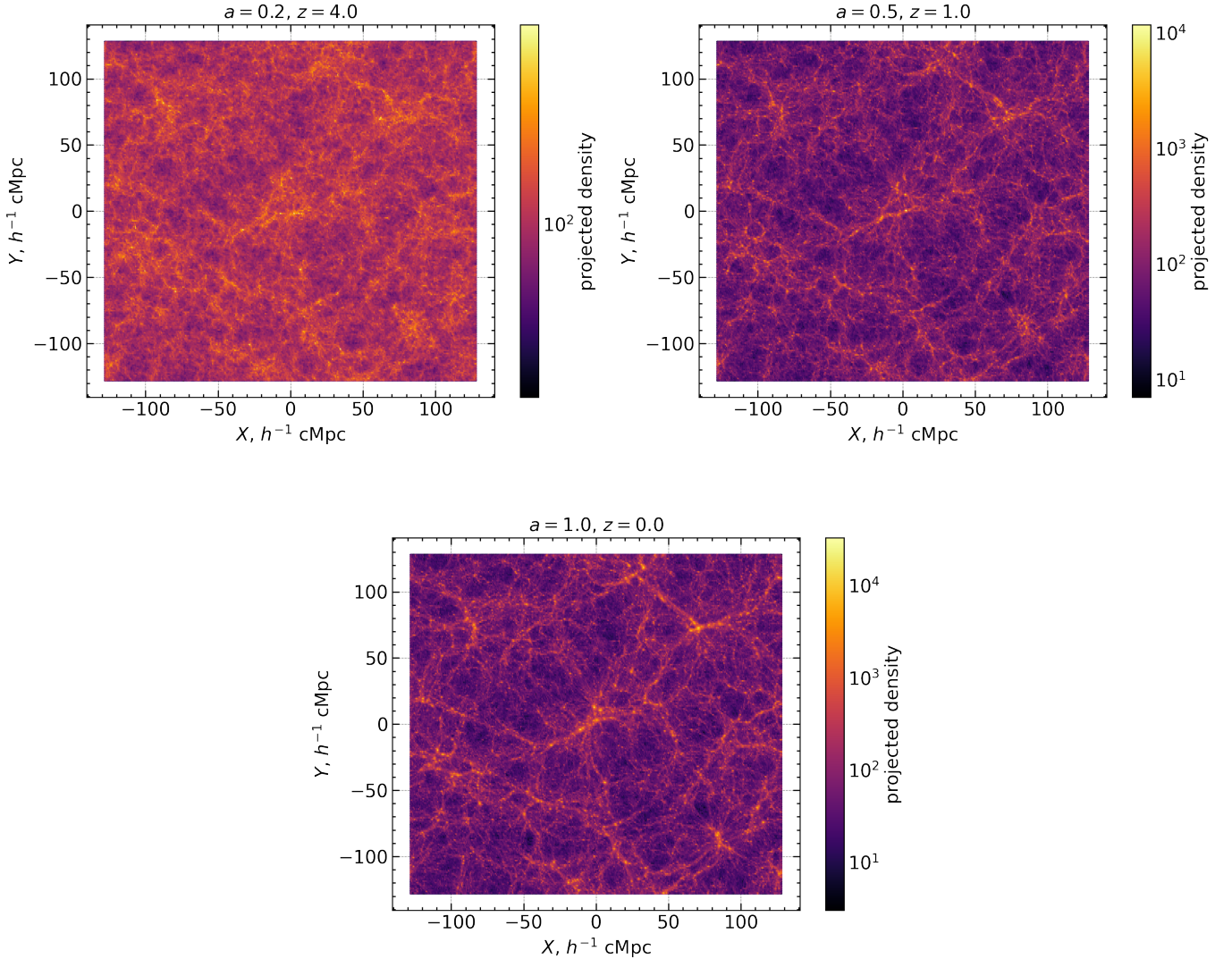


Figure 1. Projected density for a 20 Mpc deep slice through the density field of Run 4 at $a = 0.2$, $a = 0.5$ and $a = 1$.

To quantify the amount of error between measurement and theory, I calculate the transfer function $T(k) = P_{true}(k)/P(k)$. To be able to compare between runs, I first restrict k to be in the range measured by the smallest simulation and interpolate onto a grid with 50 points. Figure 6 shows the transfer functions for each run as well as the global error defined as the L2 norm of $T(k) - 1$. Here we see that while the error does get smaller with increasing N , the power spectra are not actually converging to the theory result. The simulations are exhibiting self-convergence, in the sense that the power spectra do look like they are converging to a fixed form, but they are not converging to the CCL power spectrum. This indicates some deeper differences between the GADGET simulations and the CCL calculation. This is most likely due to the fact that the GADGET initial conditions are generated from an initial power spectrum that is estimated using a simple analytic parameterization, while CCL uses the full calculation from CLASS.

Figure 7 shows the 2-point correlation functions of the FoF groups and subhalos for these runs. At large scales, these all exhibit a power law as expected. These runs do seem to show self-convergence as the correlation functions get closer as N increases. Additionally, for larger N we get more detail at smaller scales since smaller halos are able to form.

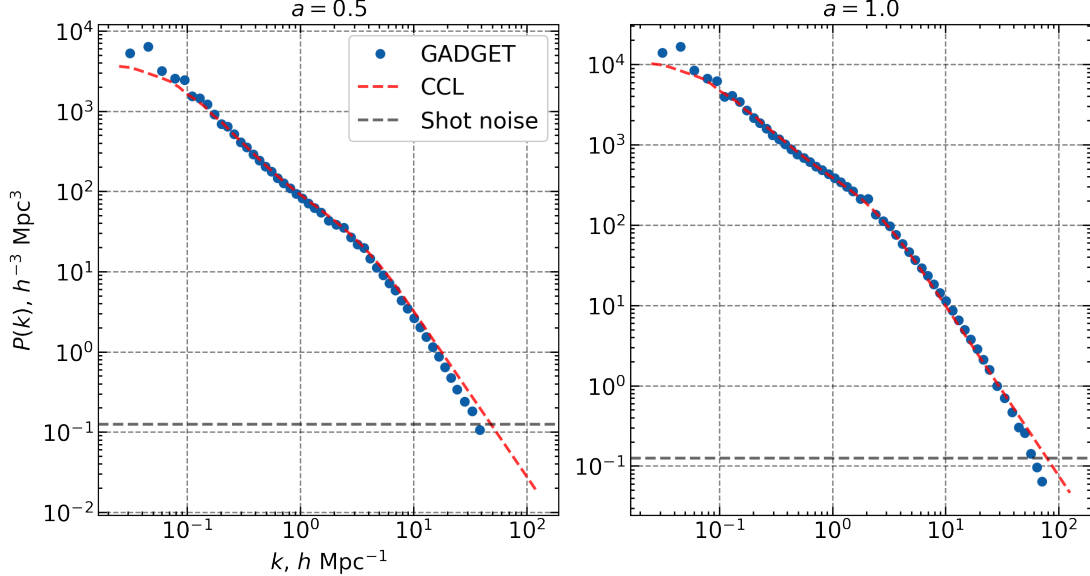


Figure 2. Matter power spectrum for Run 4 compared with the results from CCL. Note: the GADGET measurement has not been re-binned yet and so has very significant noise.

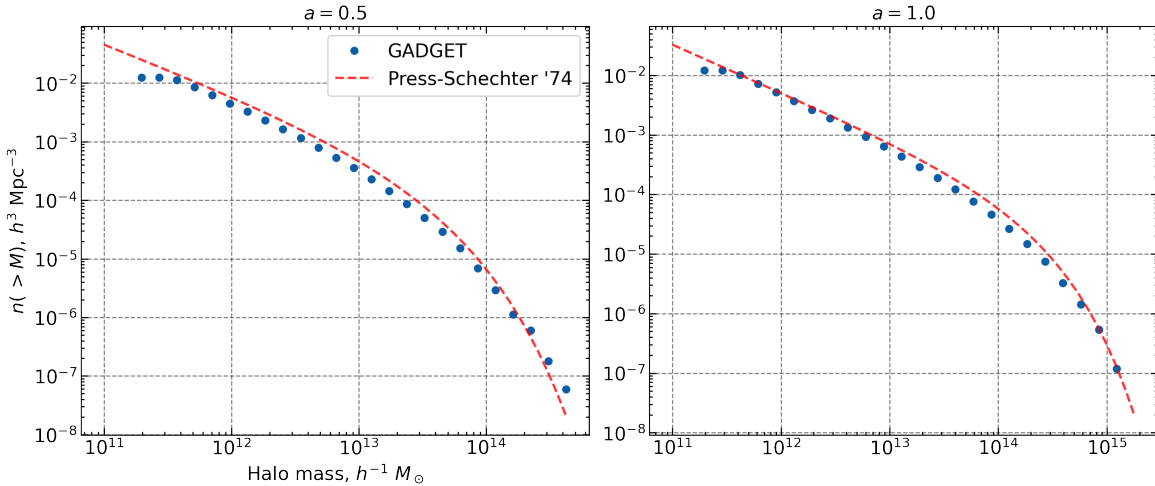


Figure 3. Halo mass function for Run 4.

5.2. Box size

Simulation runs 13, 3, 14, and 15 correspond to values of L of 512, 256, 128, and 64 Mpc respectively. Each of these runs has 256^3 particles.

Figure 8 shows the power spectra errors for these runs. Here we see two effects. First, as the box size decreases, the range over which the power spectrum is measured shifts to smaller scales. But, we do not get more accurate small scale measurements for free: as the box size decreases, we get larger errors at medium scales. This shows that a finite box size can introduce errors in the mid-scale structures by ignoring the large-scale modes just as found by Bagla & Ray (2005).

Figure 9 shows the correlation functions for these runs. Here again we do see self-convergence just like for the above runs.

5.3. Initial conditions

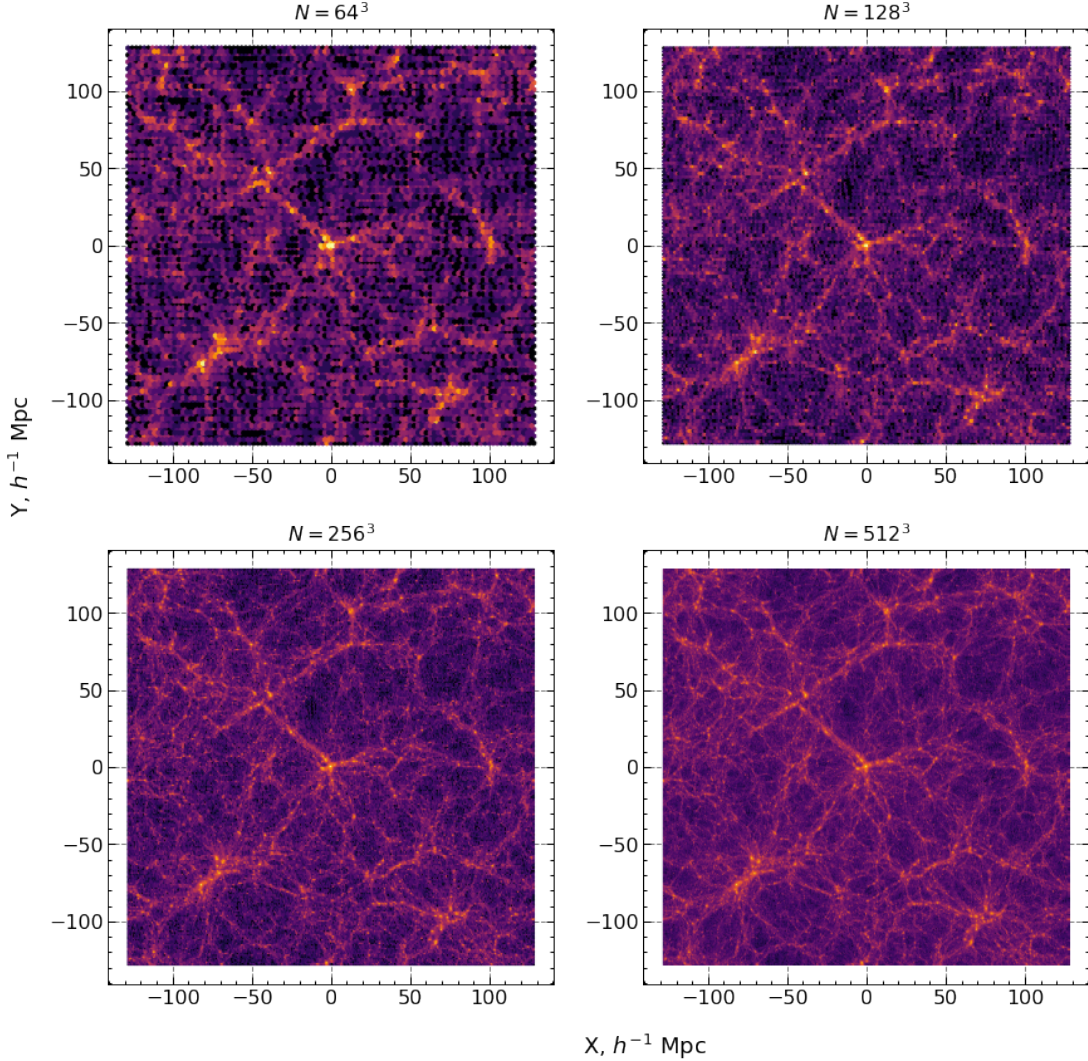


Figure 4. 20 Mpc thick slices through Runs 1-4 at $a = 1$ centered on the most massive halo in the simulation.

To look at the differences between ZA initial conditions and 2LPT initial conditions, I compare the following pairs of simulation runs: 1 and 5, 2 and 6, and 3 and 7. For each pair, I compare the errors in the matter power spectrum and the FoF HMF.

Figure 10 shows the results for the power spectra. Here I plot the transfer functions between the measured and predicted power spectra for each pair of simulation runs. For each pair, the run that uses 2LPT is consistently closer to the theory prediction than the run that uses ZA. Additionally the difference between the two methods increases at smaller scales. This is exactly what we would expect. The smaller scales become non-linear much sooner than the larger scales and so ZA, which only takes into account linear terms, introduces errors at small scales that are not present when using 2LPT.

Figure 11 shows the results for the HMFs. Here I compare the FoF HMFs of each run to the Press-Schechter HMF parameterization. Here there are not really discernible trends as there were with the power spectra, but we still see that 2LPT initial conditions generally give results that are closer to the theory predictions.

These results generally match those found by Crocce et al. (2006). They found that using 2LPT initial conditions instead of the standard ZA ones avoided errors in the form of transients arising from the ignored second-order terms. These transients cause errors in the power spectra and HMFs on the percent-level.

5.4. Softening length

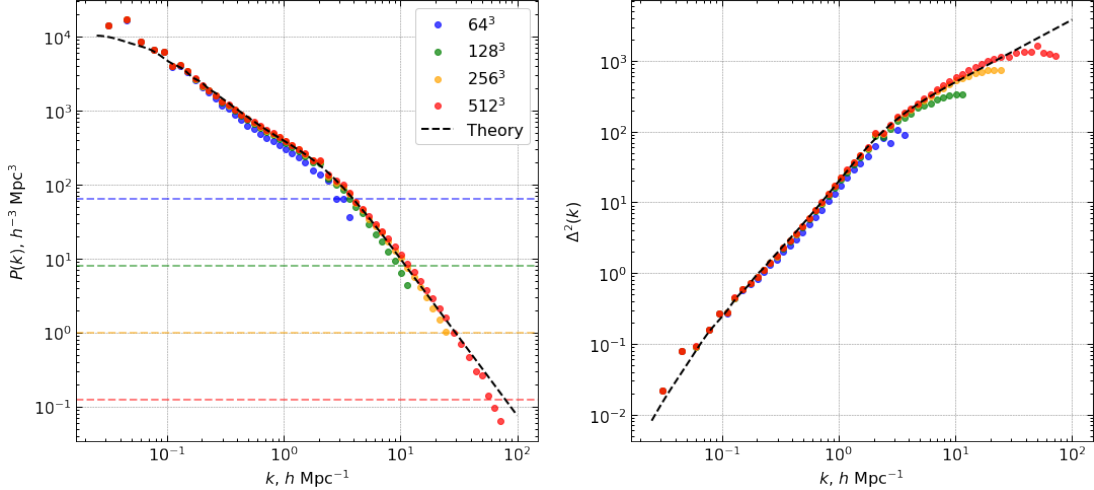


Figure 5. Matter power spectra ($P(k)$) on the left and $\Delta^2(k)$ on the right) for Runs 1-4. The colored points are the re-binned power spectra as measured by GADGET for each of the runs while the black dashed line is the theory prediction from CCL. The horizontal dashed lines indicate the shot noise level for each of the runs.

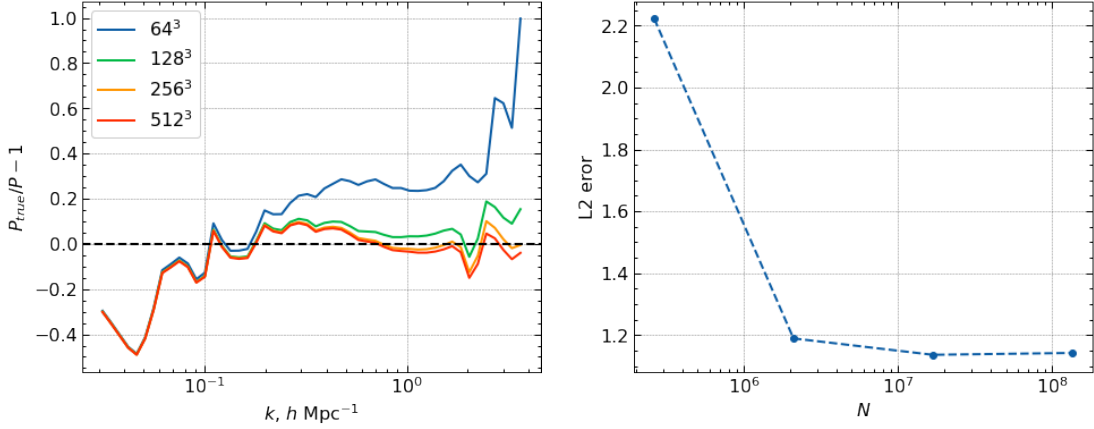


Figure 6. Errors in the measure power spectra for Runs 1-4.

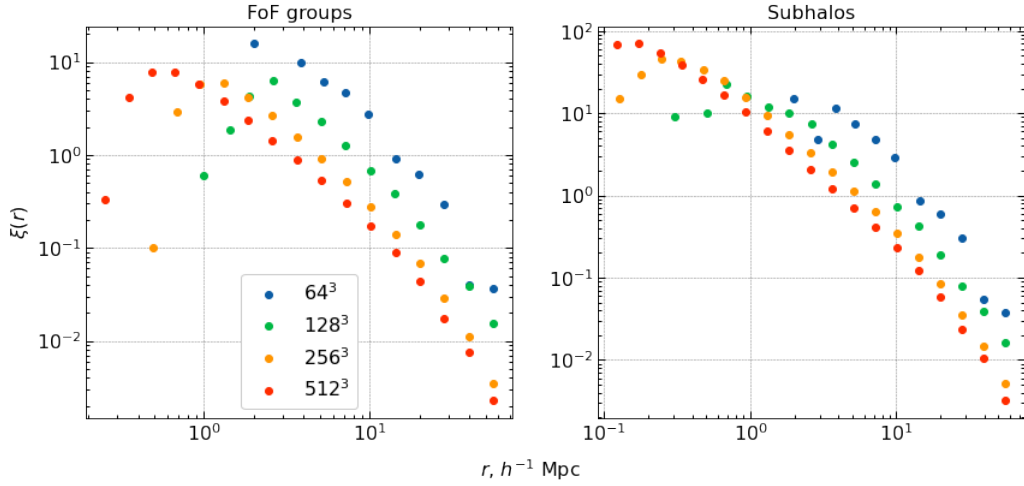


Figure 7. 2-point correlation functions of DM halos for Runs 1-4.

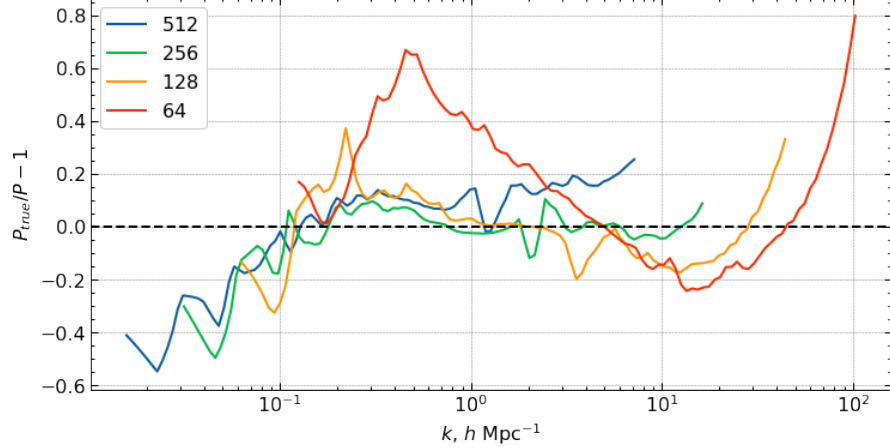


Figure 8. Transfer functions between the power spectra and the theory result for Runs 13, 3, 14, and 15. The legend indicates the value of L in Mpc for the run.

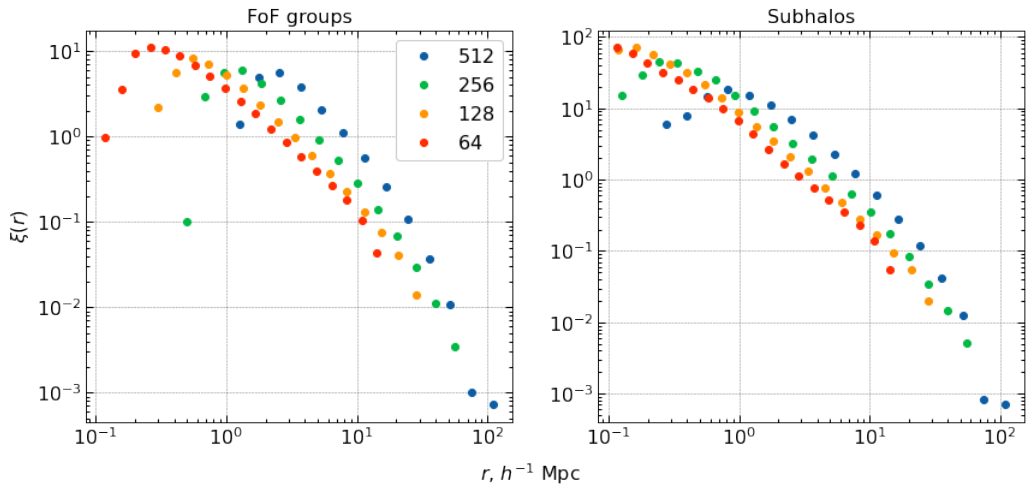


Figure 9. 2-point correlation functions of DM halos for Runs 13, 3, 14, and 15.

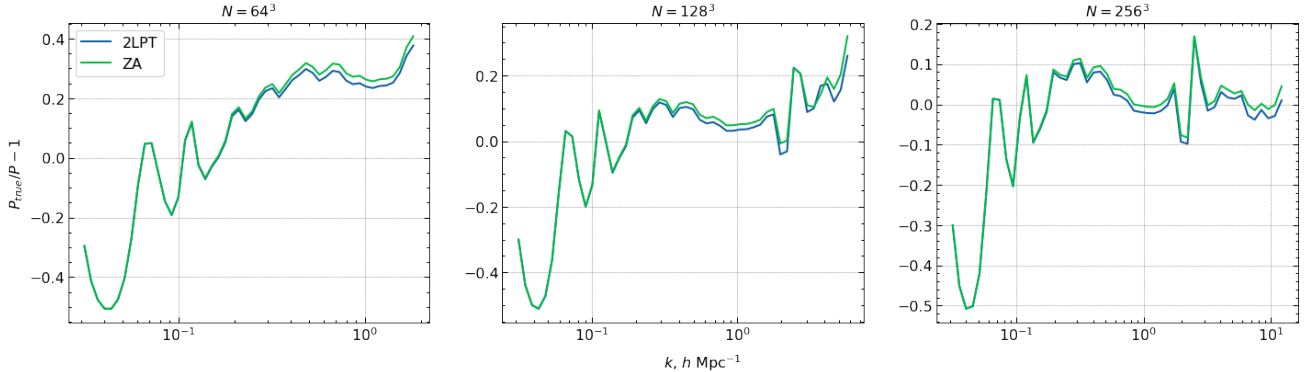


Figure 10. Power spectra errors for simulation runs using ZA and 2LPT initial conditions.

Simulation runs 8, 9, 3, 10, and 11 have increasing values of the softening length ϵ with fixed N and L . The softening length here ranges from 5 kpc for run 8 up to 45 kpc for run 11, thus there should be absolutely no difference between these runs on large scales. Here I look at the power spectra and the halo density profiles.

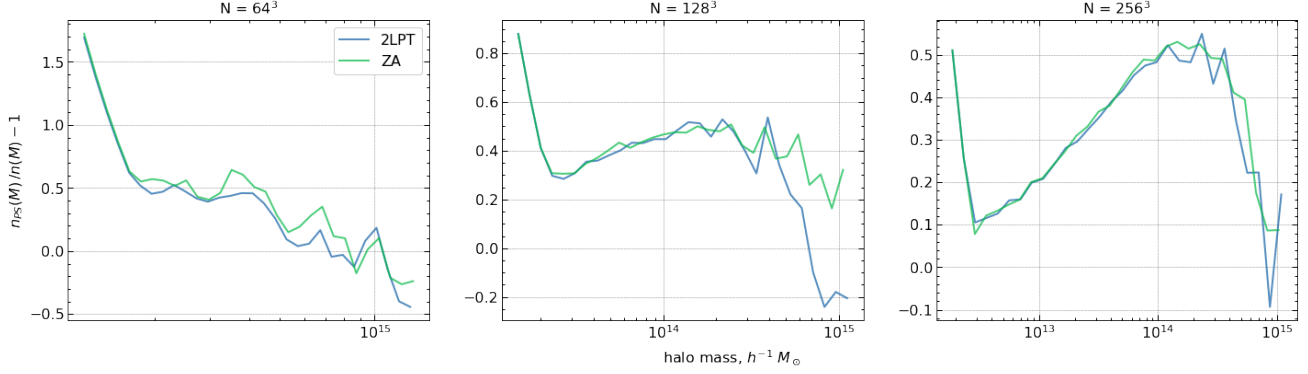


Figure 11. Halo mass function errors for simulation runs using ZA and 2LPT initial conditions.

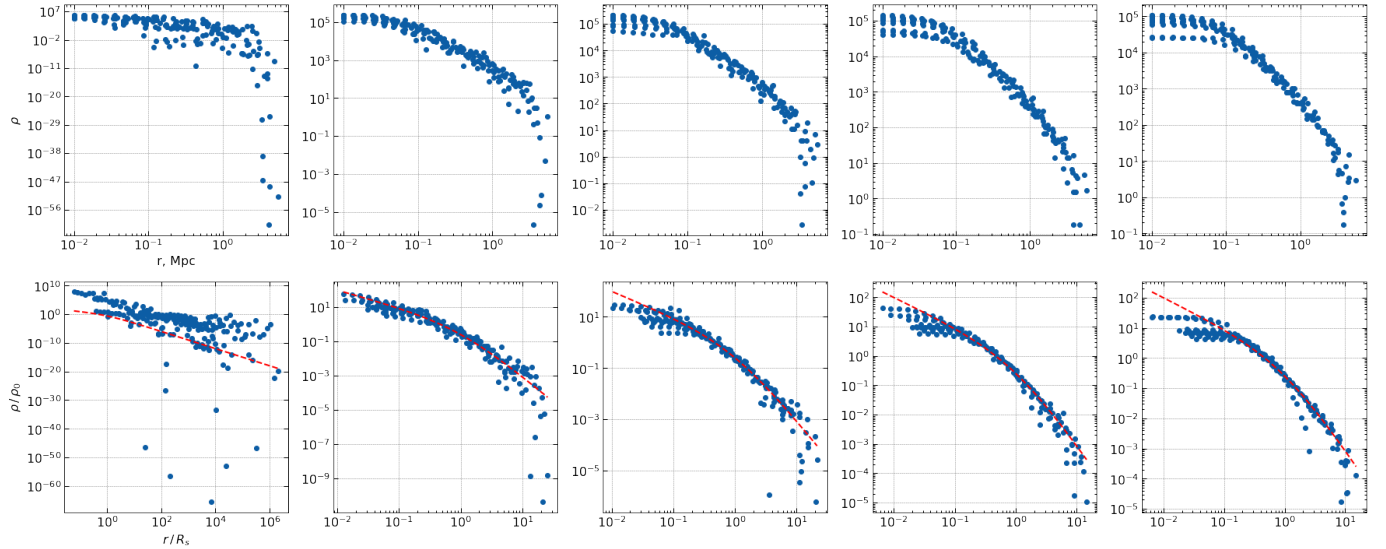


Figure 12. Radial density profiles for the ten most massive halos in simulation runs 8, 9, 3, 10, and 11. The top row shows the actual density profiles, while the bottom row shows the re-scaled profiles after fitting to a NFW profile.

Figure 13 shows the errors in the power spectra for the different values of ϵ . Just as expected, we see no difference on large scales, but the power spectra begin to diverge at smaller scales. Here Runs 3 and 10 produce power spectra closest to the theory prediction by CCL. This confirms the general rule-of-thumb used in cosmological simulations $\epsilon \approx 1/35L/N^{1/3}$ as well as the more specific recommendation from Diemer & Kravtsov (2014) where they recommend using $\epsilon = 1/42L/N^{1/3}$ for simulations with $L \sim 200$ Mpc.

Figure 1 shows the radial density profiles for the 10 most massive FoF halos in the simulations. Here we see what happens when the softening length is either too small or too large. On the far left, with $\epsilon = 5h^{-1}$ kpc, the density profiles are way too flat and do not match the NFW profile. This is because when ϵ is too small many close encounters occur in the centers of halos which causes the particles to be flung out to large radii. As we increase ϵ , the profiles become much closer to the NFW profile. But, once the softening length becomes too large the inner parts of the profiles become flat since we lose spatial resolution. These density profiles again support the choice of softening length of around 1/42 times the mean interparticle separation.

6. DISCUSSION AND CONCLUSIONS

All of the results in the previous section illustrates that there are two very important considerations that must go into the design of any cosmological simulation. First, the parameters must be chosen for the simulation to actually model the regime of interest. Second, the parameters must be sufficient to get the desired accuracy in the measured observables. An example of this is the difference between running a simulation of galaxy formation versus running one to simulate the large-scale structure. The physics that the first simulation aims to probe is dominated by small-scale

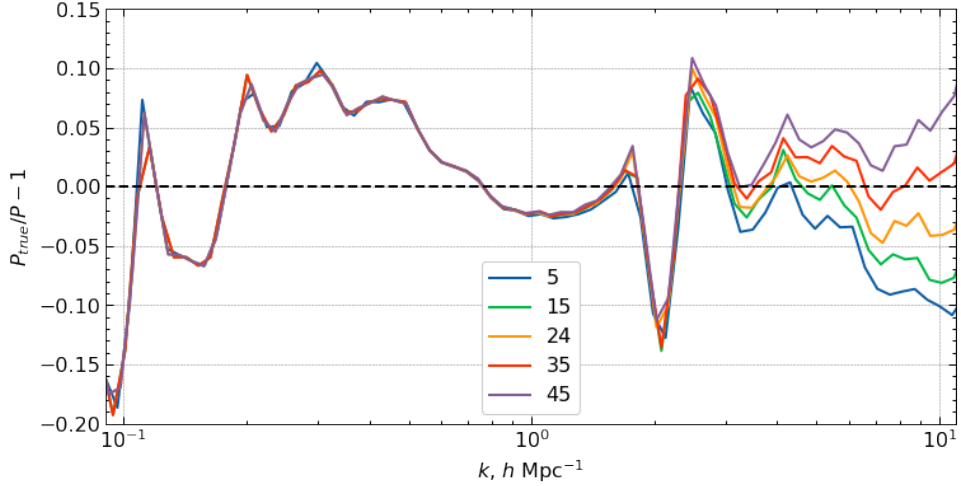


Figure 13. Power spectra errors for Runs 8, 9, 3, 10, and 11. The legend indicates the softening length used in kpc.

effects, so it would not need a huge box size as long as it is large enough to capture enough of the large-scale effects. But, the mass resolution would need to be very small in order to properly capture the formation of low-mass halos and resolve the structure inside galaxies. On the other hand, when looking at the statistics of large-scale structure, a large box size is much more important while the mass resolution does not have to be as small. After determining the regimes probed by the simulation, then it is important to make sure that N is large enough to provide accurate enough results for whatever application is needed.

Based on the analysis in previous sections, we arrive at the following conclusions for the various discretization parameters looked at in this paper.

- For initial conditions, there is essentially no reason not to use 2LPT instead of the ZA. There is almost no additional computational cost, since generation of initial conditions is a one-time step and is negligible compared to the actual simulation run. 2LPT rather saves computational effort since it allows the simulation to be started at a later redshift due to the more accurate initial particle displacements. In terms of the cosmological observables, there is a very small but noticeable difference in both the matter power spectrum and the halo mass function. Thus, for modern simulations where percent-level accuracy is needed for application to large surveys, 2LPT initial conditions are necessary.
- The particle number and box size most directly affect which regimes the simulation can model. Generally, for a cosmological simulation, L needs to be on the order of 100 Mpc to ensure that the large-scale structure forms properly. N then must be large enough that the particle masses are small enough to resolve the desired structures.
- The softening length generally has little effect on large scales, but has a very direct effect on the smallest scales of the simulation. Thus the softening length is a very important decision for any simulation that aims to probe small scales such as evolution of dark matter halos, formation of galaxies, etc. The softening length must be large enough that close encounters do not occur between particles, but small enough to allow small scales to be resolved. For the simulations tested in this work, a softening length of 1/42 to 1/30 times the mean interparticle separation is ideal.

All of this is very important to keep in mind when designing simulations that are to be compared with observational surveys. Especially with modern surveys where the statistical errors become much smaller than the systematic ones.

REFERENCES

- Abbott, T. M. C., Abdalla, F. B., Alarcon, A., et al. 2018, PhRvD, 98, 043526, doi: [10.1103/PhysRevD.98.043526](https://doi.org/10.1103/PhysRevD.98.043526)
- Alam, S., Ata, M., Bailey, S., et al. 2017, MNRAS, 470, 2617, doi: [10.1093/mnras/stx721](https://doi.org/10.1093/mnras/stx721)

- Angulo, R. E., & Hahn, O. 2022, Living Reviews in Computational Astrophysics, 8, 1, doi: [10.1007/s41115-021-00013-z](https://doi.org/10.1007/s41115-021-00013-z)
- Angulo, R. E., Springel, V., White, S. D. M., et al. 2012, MNRAS, 426, 2046, doi: [10.1111/j.1365-2966.2012.21830.x](https://doi.org/10.1111/j.1365-2966.2012.21830.x)
- Bagla, J. S., & Ray, S. 2005, MNRAS, 358, 1076, doi: [10.1111/j.1365-2966.2005.08858.x](https://doi.org/10.1111/j.1365-2966.2005.08858.x)
- Binney, J. 2004, MNRAS, 350, 939, doi: [10.1111/j.1365-2966.2004.07699.x](https://doi.org/10.1111/j.1365-2966.2004.07699.x)
- Brout, D., Scolnic, D., Popovic, B., et al. 2022, arXiv e-prints, arXiv:2202.04077. <https://arxiv.org/abs/2202.04077>
- Chisari, N. E., Alonso, D., Krause, E., et al. 2019, ApJS, 242, 2, doi: [10.3847/1538-4365/ab1658](https://doi.org/10.3847/1538-4365/ab1658)
- Colombi, S., Jaffe, A., Novikov, D., & Pichon, C. 2009, MNRAS, 393, 511, doi: [10.1111/j.1365-2966.2008.14176.x](https://doi.org/10.1111/j.1365-2966.2008.14176.x)
- Crocce, M., Pueblas, S., & Scoccimarro, R. 2006, MNRAS, 373, 369, doi: [10.1111/j.1365-2966.2006.11040.x](https://doi.org/10.1111/j.1365-2966.2006.11040.x)
- Croton, D. 2013, Publications of the Astronomical Society of Australia, 30, e052, doi: [10.1017/pasa.2013.31](https://doi.org/10.1017/pasa.2013.31)
- Diemer, B., & Kravtsov, A. V. 2014, ApJ, 789, 1, doi: [10.1088/0004-637X/789/1/1](https://doi.org/10.1088/0004-637X/789/1/1)
- Dodelson, S. 2003, Modern Cosmology (Academic Press)
- Frieman, J. A., Turner, M. S., & Huterer, D. 2008, ARA&A, 46, 385, doi: [10.1146/annurev.astro.46.060407.145243](https://doi.org/10.1146/annurev.astro.46.060407.145243)
- Garrison, L. H., Eisenstein, D. J., Ferrer, D., Maksimova, N. A., & Pinto, P. A. 2021a, MNRAS, 508, 575, doi: [10.1093/mnras/stab2482](https://doi.org/10.1093/mnras/stab2482)
- Garrison, L. H., Joyce, M., & Eisenstein, D. J. 2021b, MNRAS, 504, 3550, doi: [10.1093/mnras/stab1096](https://doi.org/10.1093/mnras/stab1096)
- Habib, S., Pope, A., Finkel, H., et al. 2016, NewA, 42, 49, doi: [10.1016/j.newast.2015.06.003](https://doi.org/10.1016/j.newast.2015.06.003)
- Heitmann, K., Finkel, H., Pope, A., et al. 2019, ApJS, 245, 16, doi: [10.3847/1538-4365/ab4da1](https://doi.org/10.3847/1538-4365/ab4da1)
- Korytov, D., Hearin, A., Kovacs, E., et al. 2019, ApJS, 245, 26, doi: [10.3847/1538-4365/ab510c](https://doi.org/10.3847/1538-4365/ab510c)
- Maleuvre, S., Eisenstein, D., Garrison, L. H., & Joyce, M. 2022, MNRAS, 512, 1829, doi: [10.1093/mnras/stac578](https://doi.org/10.1093/mnras/stac578)
- Marinacci, F., Vogelsberger, M., Pakmor, R., et al. 2018, MNRAS, 480, 5113, doi: [10.1093/mnras/sty2206](https://doi.org/10.1093/mnras/sty2206)
- Naiman, J. P., Pillepich, A., Springel, V., et al. 2018, MNRAS, 477, 1206, doi: [10.1093/mnras/sty618](https://doi.org/10.1093/mnras/sty618)
- Navarro, J. F., Frenk, C. S., & White, S. D. M. 1997, ApJ, 490, 493, doi: [10.1086/304888](https://doi.org/10.1086/304888)
- Nelson, D., Pillepich, A., Springel, V., et al. 2018, MNRAS, 475, 624, doi: [10.1093/mnras/stx3040](https://doi.org/10.1093/mnras/stx3040)
- Peebles, P. J. E. 1980, The large-scale structure of the universe (Princeton University Press)
- Pillepich, A., Nelson, D., Hernquist, L., et al. 2018, MNRAS, 475, 648, doi: [10.1093/mnras/stx3112](https://doi.org/10.1093/mnras/stx3112)
- Planck Collaboration, Aghanim, N., Akrami, Y., et al. 2020, A&A, 641, A6, doi: [10.1051/0004-6361/201833910](https://doi.org/10.1051/0004-6361/201833910)
- Power, C., & Knebe, A. 2006, MNRAS, 370, 691, doi: [10.1111/j.1365-2966.2006.10562.x](https://doi.org/10.1111/j.1365-2966.2006.10562.x)
- Power, C., Navarro, J. F., Jenkins, A., et al. 2003, MNRAS, 338, 14, doi: [10.1046/j.1365-8711.2003.05925.x](https://doi.org/10.1046/j.1365-8711.2003.05925.x)
- Press, W. H., & Schechter, P. 1974, ApJ, 187, 425, doi: [10.1086/152650](https://doi.org/10.1086/152650)
- Quinn, T., Katz, N., Stadel, J., & Lake, G. 1997, arXiv e-prints, astro. <https://arxiv.org/abs/astro-ph/9710043>
- Riess, A. G., Yuan, W., Macri, L. M., et al. 2021, arXiv e-prints, arXiv:2112.04510. <https://arxiv.org/abs/2112.04510>
- Scoccimarro, R. 1998, MNRAS, 299, 1097, doi: [10.1046/j.1365-8711.1998.01845.x](https://doi.org/10.1046/j.1365-8711.1998.01845.x)
- Springel, V. 2005, MNRAS, 364, 1105, doi: [10.1111/j.1365-2966.2005.09655.x](https://doi.org/10.1111/j.1365-2966.2005.09655.x)
- Springel, V., Pakmor, R., Zier, O., & Reinecke, M. 2021, MNRAS, 506, 2871, doi: [10.1093/mnras/stab1855](https://doi.org/10.1093/mnras/stab1855)
- Springel, V., White, S. D. M., Tormen, G., & Kauffmann, G. 2001a, MNRAS, 328, 726, doi: [10.1046/j.1365-8711.2001.04912.x](https://doi.org/10.1046/j.1365-8711.2001.04912.x)
- Springel, V., Yoshida, N., & White, S. D. M. 2001b, NewA, 6, 79, doi: [10.1016/S1384-1076\(01\)00042-2](https://doi.org/10.1016/S1384-1076(01)00042-2)
- Springel, V., Pakmor, R., Pillepich, A., et al. 2018, MNRAS, 475, 676, doi: [10.1093/mnras/stx3304](https://doi.org/10.1093/mnras/stx3304)
- Tinker, J., Kravtsov, A. V., Klypin, A., et al. 2008, ApJ, 688, 709, doi: [10.1086/591439](https://doi.org/10.1086/591439)
- Turner, M. S. 2022, arXiv e-prints, arXiv:2201.04741. <https://arxiv.org/abs/2201.04741>
- Verde, L., Treu, T., & Riess, A. G. 2019, Nature Astronomy, 3, 891, doi: [10.1038/s41550-019-0902-0](https://doi.org/10.1038/s41550-019-0902-0)
- Villaescusa-Navarro, F., Anglés-Alcázar, D., Genel, S., et al. 2021, ApJ, 915, 71, doi: [10.3847/1538-4357/abf7ba](https://doi.org/10.3847/1538-4357/abf7ba)
- Warren, M. S., Abazajian, K., Holz, D. E., & Teodoro, L. 2006, ApJ, 646, 881, doi: [10.1086/504962](https://doi.org/10.1086/504962)
- Zel'dovich, Y. B. 1970, A&A, 5, 84